

Supplementary information for the paper

## Structural Cause of Missed Eruption in the Lunayyir Basaltic Field (Saudi Arabia) in 2009

Koulakov, I., El Khrepy, S., Al-Arifi, N., Kuznetsov, P., and Kasatkina, E.

### **Supplementary 1: Data analysis and algorithm details**

For the inversion, we selected the events that had a combined number of P- and S-picks  $\geq 8$ . We have defined a threshold for the residuals of 0.4 s for P-wave data and 0.7 for S-wave data, that reflected the upper limit of expected time delays due to velocity anomalies. The initial residuals were computed by locating events in a large number of different 1-D models having a fixed constant value for  $V_p/V_s$  and defined P-velocities at several depth levels. Between these levels, velocity was linearly approximated. For each model, we examined the number of data point having residuals below the predefined threshold. The model that enabled the maximum value was selected as a starting model for the tomographic inversion. In the best model derived for our case,  $V_p/V_s$  was equal to 1.7, and the P-wave velocities were defined as follows: 5.6 km/s at an altitude of 2 km above sea level, 6.0 km/s at 10 km below sea level (bsl), and 7.0 km/s at 30 km bsl. The final tomography model was constructed based on 5847 P-wave rays and 7096 S-wave rays from 1326 events. The high quality of the data is evidenced by relatively low RMS values of the initial residuals, and their strong reduction during the tomographic inversion. Initially, the residuals after location in the 1-D model were as high as 0.157 s and 0.205 s for the P- and S-wave data, respectively. After five iterations of the 3-D inversion, the residuals were reduced to 0.0547 and 0.0576 s (65.2% and 71.9% of variance reduction), respectively. The final numbers appear to be close to the estimated accuracy of the picking for the P- and S-wave data.

For the tomographic inversion, we used the LOTOS code by Koulakov (2009). The calculations start with the preliminary locations of events by using tabulated values of travel times corresponding to all combinations of epicentral distances and depths of events. The next step locates the sources via a 3-D ray-tracing algorithm based on the bending method. The unknown 3-D velocity distribution is parameterized using a node mesh. In map view, the nodes are installed according to a regular grid with a predefined spacing (2 km in our case) only in areas where there are rays. In the vertical direction, the spacing between the nodes depends on the density of rays, but it cannot be smaller than a predefined value (1 km in our case). To avoid artifacts related to the predefined grid orientation, we performed the inversions for four grids with different basic orientations (0, 22, 45, and 67 degrees). The inversion of the matrix was performed simultaneously for P- and S-wave anomalies, source parameters (dx, dy, dz, and dt for each source), and station corrections. The inversion of the matrix was performed using the LSQR method (Nolet, 1987; Paige and Saunders, 1982). The stability of the solution was controlled by damping gradients of velocity variations between neighboring nodes. The values of the smoothing coefficients and the weights for the source and station parameters were determined according to the results of synthetic modeling.

### **Supplementary 2: Synthetic modeling**

The synthetic modeling is performed for the same ray configurations as presented in the case of observed data processing. After computing the synthetic travel times using 3D ray tracing, we “forget” the locations of the sources. We perform the calculations using an identical workflow as the observed data inversion. In particular, we start the processing with the location of sources in the 1D model, which strongly biases the source coordinates and perturbs the synthetic residuals. As a result, we face the same problem that exists when processing the observed data, i.e., the trade-off between source and velocity solutions, which may strongly smear the reconstructed anomalies.

We present synthetic tests aimed at the separate analysis of the horizontal and vertical resolutions. Figure S1 shows the results of three tests with checkerboards defined as unlimited vertical columns. The amplitudes of the anomalies in all cases are  $\pm 8\%$ , and the signs of the P- and S-wave anomalies are opposite to create strong variations in the  $V_p/V_s$  ratio. The random noise added to the data was similar for the P and S data (0.05 s of average deviation). We performed the reconstruction of the synthetic model using absolutely identical workflow as in the case of observed data analysis. After inversion, we obtained 50-55% of variance reduction and  $\sim 0.06$  s of the final residual average deviations for the P and S data, that is similar to the case of inversion of experimental data. We observe that the reconstructed anomalies in all cases are resolved at correct locations. However, their amplitudes and shapes are strongly biased. It is interesting that the  $V_p/V_s$  ratio model, which is obtained by a simple division of the resulting P- and S-wave velocities, reveals the structures even more clearly than the separate P- and S-wave models. This finding proves the adequacy of this manner of ratio computing.

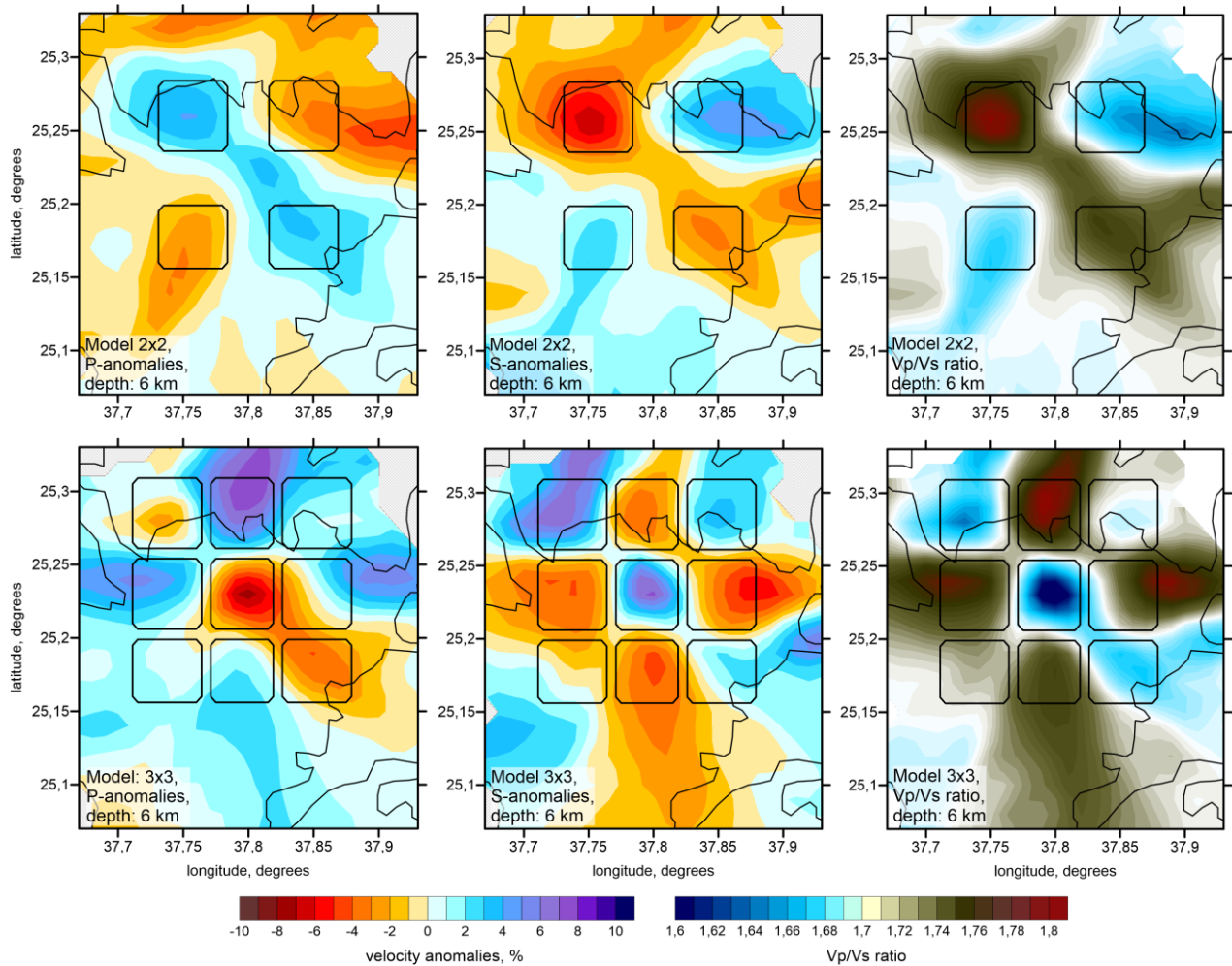


Figure S1. Checkerboard tests with three different synthetic models marked with black lines for P- and S-wave anomalies and Vp/Vs ratios. All results are presented at 6 km depth.

In Figure S2, we present several tests showing the vertical resolution along three profiles, which are the same as those used for visualizing the results in Figure S4. Three types of patterns were defined in each of the three profiles in a vertical layer of 6 km thickness centered on the corresponding profile (all nine models were computed separately). Here, we demonstrate only the Vp/Vs ratio results in order to save space and because this parameter is of greatest interest for interpretation in our case. Unlike most of our previous studies exhibiting considerably poorer vertical resolution, we observe here that the vertical anomalies are resolved similarly as in the horizontal sections. For example, for models 2 and 3, we

robustly detect the transition of the anomaly sign at 4 km depth. For the three-layered model (upper row in Figure S2), we can clearly identify the transition at 7 km depth, but the shallowest layer is not well resolved. For all models, we see rather strong smearing of the anomalies in marginal areas.

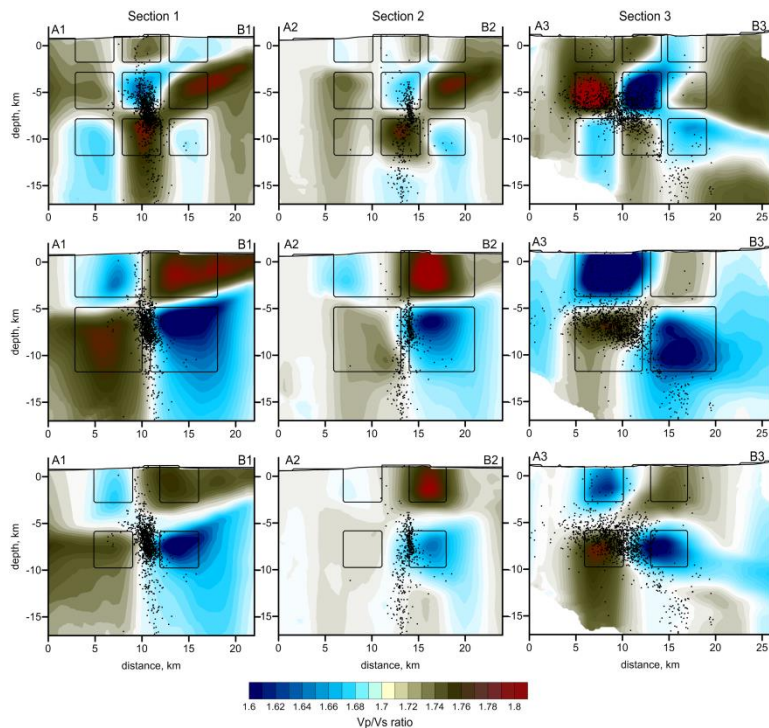


Figure S2. Reconstructions of nine synthetic models corresponding to three vertical sections (the same configuration is used to present the main results in Figure S4) and three different models for each section. Here, only the reconstructed  $V_p/V_s$  ratio distributions are presented. The black lines highlight the configuration of the synthetic patterns. The black dots are the event hypocenters located at distances of less than 4 km from the profile.

### Supplementary 3: Resulting seismic models (velocity and attenuation)

The results of the observed data inversion are presented in horizontal sections (Figure S3) and in vertical sections (Figure S4). We present the anomalies of the P- and S-wave velocities, the  $V_p/V_s$  ratios and the final locations of the sources determined by the 3D

velocity model. For reference, in the horizontal sections, we show the contours of the basaltic field and the locations of the cinder cones, which are the same as those presented in Figure 1B of the main paper. The velocity anomalies are in the range of  $\pm 5\%$ ; these are relatively small amplitudes compared to other volcanic areas. However, it should be taken into account that the anomalies might be smeared; thus, their amplitudes may be significantly diminished. The synthetic results show that the amplitudes of the reconstructed anomalies are approximately half those of the “true” synthetic values. The  $V_p/V_s$  ratios vary from 1.6 to 1.8, but this range in reality might be broader for the same reason.

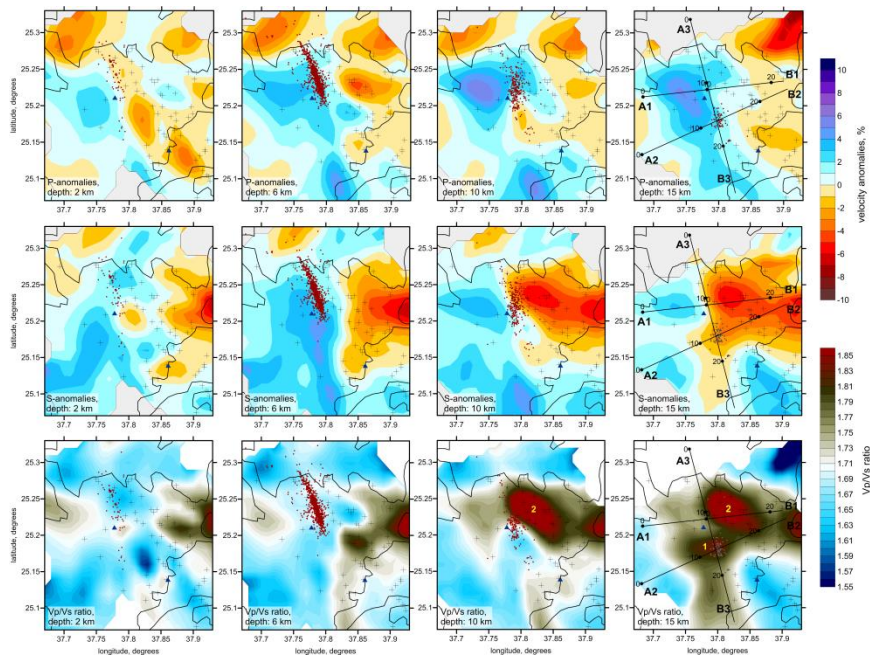


Figure S3. Results of the observed data inversion in horizontal sections. The distributions of P- and S-wave anomalies and  $V_p/V_s$  ratios are presented. The black line indicates the limit of the basalt field (same as in Figure 1). The black crosses mark the volcanic cones. The brown dots are the events in the corresponding depth intervals. Yellow numbers 1 and 2 indicate the structures discussed in the text.

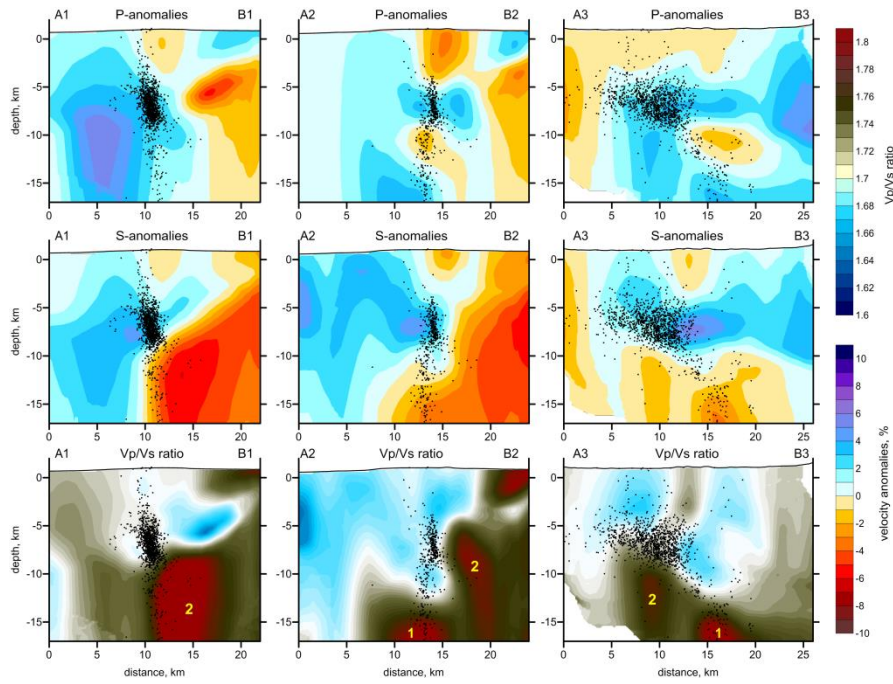


Figure S4. Results of the observed data inversion in the three vertical sections with the locations shown in Figure 5. The distributions of P- and S-wave anomalies and Vp/Vs ratios are presented. The black dots are projections of the events located at distances of less than 4 km from the profile. Yellow numbers 1 and 2 indicate the structures discussed in the text.

In Figure S5, we present the recent results of the attenuation tomography described by Koulakov *et al.* (2014). Here, we show the vertical sections of the 3D attenuation model using the same profiles as in Figure 6. To facilitate the comparison of the models, in Figure S5, we plot the same earthquakes as in Figure S4. The events used for the attenuation tomography were slightly different. It can be seen that the main features of the attenuation model fit the velocity model. In particular, we see that in Section 1, to the right side of the seismicity cluster, there is a clear anomaly of higher attenuation, which is consistent in location with anomaly “2.” In Section 2, both anomalies “1” and “2” are detectable in the attenuation model. In Section 3, anomaly “1” appears clearer in the attenuation results; anomaly “2” is also visible, though less prominently than in the velocity model. For the shallower levels, the low-attenuation areas correspond to anomalies of higher velocities and

lower  $V_p/V_s$  ratios in the velocity model. The clear correlation of the attenuation and velocity tomography results also supports the robustness of the derived models.

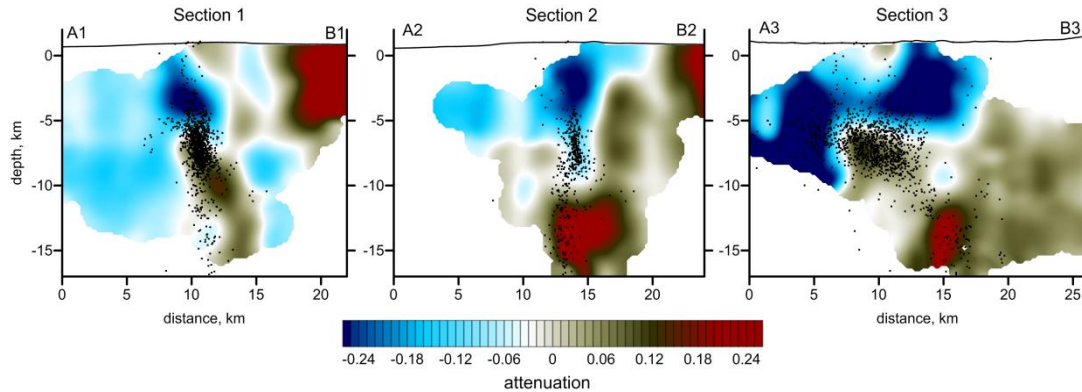


Figure S5. Results of the attenuation tomography from Koulakov *et al.* (2014) presented in the same vertical sections as in Figure 6. The dots are the earthquake locations used in this study and are provided for reference.

## References

- Koulakov, I., 2009, LOTOS code for local earthquake tomographic inversion. Benchmarks for testing tomographic algorithms: *Bulletin of the Seismic Society of America*, v. 99, p. 194–214, doi:10.1785/0120080013.
- Koulakov I., El Khrepy, S., Al-Arifi, N., Sychev, I., Kuznetsov, P., 2014, Evidence of magma activation beneath the Lunayyir basaltic field (Saudi Arabia) from attenuation tomography. *Solid Earth*, v. 5, p. 873-882, doi:10.5194/se-5-1-2014.
- Nolet, G., 1987, *Seismic wave propagation and seismic tomography*, in Nolet, G., ed., *Seismic Tomography*: Dordrecht, Netherlands, Reidel, p. 1–23.
- Paige, C.C., and Saunders, M.A., 1982, LSQR: An algorithm for sparse linear equations and sparse least squares: *ACM Transactions on Mathematical Software*, v. 8, p. 43–71, doi:10.1145/355984.355989.